_ISIJINT-2023-437

Second proof | Stamp

ISIJ International, Vol. 64 (2024), No. 7, pp. 1–9
https://doi.org/10.2355/isijinternational.ISIJINT-2023-437

Effects of the Cr and Ni Concentrations on the Fatigue and Corrosion Resistances of Fe–Mn–Cr–Ni–Si Alloys for Seismic Damping Applications

Fumiyoshi YOSHINAKA,[1] Yusuke TSUTSUMI,[1] Tomoya NAGIRA,[1] Susumu TAKAMORI,[1] Satoshi EMURA,[1] Takahiro SAWAGUCHI,[1]* Hideki KATAYAMA,[1] Terumi NAKAMURA,[1] Yasuhiko INOUE,[2] Susumu MOTOMURA[2] and Atsumichi KUSHIBE[2]

1) National Institute for Materials Science, 1-2-1 Sengen, Tsukuba, Ibaraki, 305-0047 Japan.
2) Takenaka Corporation, 1-5-1, Otsuka, Inzai, Chiba, 270-1395 Japan.

(*Received November 21, 2023; Accepted March 4, 2024; Advance online published March 14, 2024; Published May 15, 2024*)

Previous research has shown that Fe–Mn–Cr–Ni–Si alloys offer excellent low-cycle fatigue resistance via reversible bidirectional transformation between face-centered cubic (FCC) γ-austenite and hexagonal closed-packed (HCP) ε-martensite. The alloy shows superior low-cycle fatigue life and is used for seismic damping applications, but there have been concerns over their resistance to highly corrosive environments. In this study, Fe–15Mn–*a*Cr–*b*Ni–4Si alloys were prepared with different Cr and Ni concentrations to evaluate the effects on the fatigue and corrosion resistances: Z1 with (*a*, *b*) = (14, 10.1), Z2 with (*a*, *b*) = (12.5, 8.8), Z3 with (*a*, *b*) = (11, 7.5), Z4 with (*a*, *b*) = (9.5, 6.1), and Z5 with (*a*, *b*) = (8, 4.8). Z2 had the longest fatigue life. The alloy showed Gibbs free energy difference between γ-austenite and ε-martensite phases close to the ideal of zero and the α'-martensitic transformation was suppressed well, which agreed with the design criteria for achieving bidirectional transformation-induced plasticity. The developed alloys showed superior corrosion resistance in seawater. Local pitting corrosion was observed that was attributed to the high Mn concentration of the alloys, although this was greatly mitigated by adjusting the Cr and Ni concentrations, especially with Z1 and Z2.

KEY WORDS: fatigue; steel; microstructure; martensitic transformation; corrosion resistance.

1. Introduction

Vibration-controlled structures are a design concept where the seismic energy input to a building is consumed via a damping element (*i.e.*, seismic damper) to reduce the vibration and prevent serious damage to the principal structural members.[1] Hysteretic dampers utilize an energy absorption and dissipation mechanism associated with cyclic elastoplastic deformation, and they are typically made from steel, known as steel damper.[2] Because steel dampers work by cyclic plastic deformation, they need to be made from steel with a lower yield point than the steel used in principal structural members. However, the repeated plastic deformations mean that the service life of the damper depends on its resistance to low-cycle fatigue. For high-rise buildings or long-span bridges subjected to long-period and long-term ground motions from giant earthquakes, steel dampers made from general low-yield-point steel are generally considered insufficient as a countermeasure. Therefore, research has been ongoing to develop steel alloys with excellent low-cycle fatigue resistance.[3–6]

In the literature, the relationship between the low-cycle fatigue life N_f and total strain range $\Delta\varepsilon_t$ is generally accepted to not strongly depend on the type of steel.[7] Recently, however, researchers have reported that some advanced high-strength steels (AHSSs) and high-entropy alloys (HEAs) have superior low-cycle fatigue resistance owing to the transformation-induced plasticity (TRIP) or twinning-induced plasticity (TWIP) effects.[8–15] We previously reported that a new TRIP mechanism called bidirectional TRIP (B-TRIP)[16,17] where the reversible bidirectional transformation between face-centered cubic (FCC) γ-austenite and hexagonal closed-packed (HCP) ε-martensite is effective at improving the low-cycle fatigue life.[5,18] The phase transformation is responsible for the Schockley partial dislocation, and its highly reversible nature may retard the accumulation of fatigue damage. The importance of reverse motion of dislocations, including

* Corresponding author: E-mail: Sawaguchi.takahiro@nims.go.jp

reverse transformation, has been emphasized in literature.[19] Shams *et al.*[15] and Bahadur *et al.*[20] reported the bidirectional transformation of HEAs under fatigue loading. We utilized B-TRIP to develop a Fe–15Mn–10Cr–8Ni–4Si B-TRIP alloy; it demonstrated excellent fatigue resistance with $N_f > 10\,000$ cycles at a total strain amplitude of 1%.[4] This alloy has already been applied in a high-rise building and an international exhibition hall.[21,22] However, this alloy has a high solidification cracking susceptibility, and special care is required for welding. Therefore, the alloy was modified to Fe–15Mn–11Cr–7.5Ni–4Si for reduced solidification cracking susceptibility with comparable fatigue resistance.[6]

In addition to fatigue, another important mechanism for the damage and deterioration of steel structures is corrosion.[23–26] In particular, steel dampers in a corrosive environment, such as buildings or bridges near the shore or at sea, must have high corrosion resistance in addition to the general application of antirust paint.[27,28]

The objective is to develop a new alloy with exceptional fatigue durability, whilst focusing on the impact of alloying elements that intimately associated with corrosion resistance; Cr and Ni. Fe–15Mn–*a*Cr–*b*Ni–4Si alloys were prepared where the Cr and Ni concentrations (*a* and *b*, respectively) were systematically varied so that the Cr_{eq}/Ni_{eq} ratio was approximately equal to that of the Fe–15Mn–11Cr–7.5Ni–4Si alloy that exhibited Ferrite-Austenite (FA) mode solidification that can reduce the solidification cracking susceptibility.[6] Cr and Ni both increase the corrosion resistance of stainless steels; Cr forms a passive film, and Ni reinforces the stability of the film.[23,29] Experiments were performed to investigate the effects of Cr and Ni on the phase transformation, fatigue, and corrosion behaviors of the prepared alloys.

2. Background

The chemical composition of a B-TRIP steel alloy needs to satisfy the following conditions to ensure its fatigue resistance and weldability. First, a high fatigue resistance requires balancing the thermodynamic stability of γ-austenite and ε-martensite to allow for bidirectional transformation. This condition can be written by setting the Gibbs free energy difference between γ-austenite and ε-martensite $\Delta G^{\gamma\to\varepsilon}$ as close to zero as possible (*i.e.*, $\Delta G^{\gamma\to\varepsilon} \approx 0$). $\Delta G^{\gamma\to\varepsilon}$ is calculated as follows:

$$\Delta G^{\gamma\to\varepsilon} = \Delta G^{\gamma\to\varepsilon}_{chem} + \Delta G^{\gamma\to\varepsilon}_{mag} \quad \text{..... (1)}$$

Further details are presented in the previous work.[30]

Next, the formation of body-centered cubic (BCC) α'-martensite should be prevented.[5] This is because the α'-martensitic transformation involves a volume change and thus is irreversible while the ε-martensitic transformation to ε-martensite is an almost volume-constant process. In B-TRIP alloys, the γ-austenite phase is sufficiently stable against α'-martensite to prevent the $\gamma\to\alpha'$-martensitic transformation. However, two-stage $\gamma\to\varepsilon\to\alpha'$-martensitic transformation can occur during fatigue deformation, albeit slight.

To ensure weldability, the solidification mode should be FA to reduce the susceptibility to solidification cracking.[6] This is the same policy used for stainless steels.[31,32] To control the solidification mode, the ratio of Cr equivalent (Cr_{eq}) to Ni equivalent (Ni_{eq}) can be used as a design parameter. Cr_{eq} and Ni_{eq} are calculated as follows:[33]

$$Cr_{eq} = \text{wt.\%Cr} + \text{wt.\%Mo} + 1.5\text{wt.\%Si} + 0.5\text{wt.\%Nb} \text{ ... (2)}$$

$$Ni_{eq} = \text{wt.\%Ni} + 0.5\text{wt.\%Mn} + 30\text{wt.\%C} \text{ ..... (3)}$$

In situ observation of the solidification process during welding was conducted by using synchrotron radiation X-ray imaging at SPring-8.[34,35] Fe–15Mn–10Cr–8Ni–4Si exhibited austenite (A) mode solidification and cracking while Fe–15Mn–11Cr–7.5Ni–4Si showed FA mode solidification and no crack propagation.

3. Methods

Differential scanning calorimetry (DSC) was used to characterize the thermal martensitic transformation of the prepared specimens. Axial strain-controlled fatigue tests were conducted to examine the low-cycle fatigue resistance. The deformation microstructure was analyzed by using X-ray diffraction (XRD), electron backscattering diffraction (EBSD), energy-dispersive X-ray spectroscopy (EDS), and a ferrite scope to evaluate the fatigue mechanism in terms of the microstructure. The corrosion resistance was investigated by electrochemical and non-electrochemical methods: an anodic polarization test and salt spray test, respectively.

3.1. Materials

Alloys were prepared with a nominal composition of Fe–15Mn–*a*Cr–*b*Ni–4Si according to weight percentage: Z1 with (*a*, *b*) = (14, 10.1), Z2 with (*a*, *b*) = (12.5, 8.8), Z3 with (*a*, *b*) = (11, 7.5), Z4 with (*a*, *b*) = (9.5, 6.1), Z5 with (*a*, *b*) = (8, 4.8). Z3 had the same composition as the previously reported material.[6] The alloy materials were melted in an argon environment to obtain a square frustum-shaped ingot that was forged at 1 100°C, rolled at 500°C, and heat-treated at 1 000°C for 1 h followed by water quenching. **Table 1** lists the actual chemical compositions of the alloys, which were measured by inductively coupled plasma atomic emission spectrophotometry (CIROS-120EOP, Rigaku Corporation, Japan). Z1 had the highest concentrations of Cr and Ni, followed by Z2 and so on. The contributions of Cr and Ni to corrosion resistance appeared to decrease with increasing concentrations. The Cr_{eq}/Ni_{eq} ratios as calculated by Eqs. (2) and (3) had a range of 1.13–1.15 for all alloys with Z3 having the lowest value and Z5 the highest. As noted above, synchrotron radiation measurement at SPring-8

Table 1. Chemical compositions (wt%) of the Fe–15Mn–aCr–bNi–4Si alloys [(a, b) = (14, 10.1), (12.5, 8.8), (11, 7.5), (9.5, 6.1), (8, 4.8)].

Alloy	Fe	Mn	Cr	Ni	Si	Cr_{eq}/Ni_{eq}	$\Delta G^{\gamma\to\varepsilon}$ [J/mol]	Γ_{SFE} [mJ/m^2]
Z1	Bal.	15.1	14.0	10.0	4.06	1.14	34.4	21.04
Z2	Bal.	15.0	12.5	8.74	4.06	1.14	−13.4	18.21
Z3	Bal.	15.0	11.0	7.53	4.00	1.13	−61.0	15.39
Z4	Bal.	15.0	9.48	6.12	4.08	1.15	−117.1	12.07
Z5	Bal.	14.9	8.00	4.83	4.11	1.15	−172.7	8.78

revealed that Z3 solidified in FA mode.[34,35] Synchrotron radiation measurements were also performed on Z5 to confirm whether all alloys in this study solidified in FA mode. **Figure 1** shows the (a) synchrotron radiation X-ray radiograph and (b), (c) diffraction patterns obtained as Z5 solidified during spot welding. Z5 was observed to solidify in FA mode based on the following features: primary columnar δ-ferritic dendrites grew from the weld pool boundary to the center, and the secondary equiaxed γ-austenitic dendrites nucleated in front of the columnar dendrites. Therefore, Z1–Z5 was concluded to all solidify in FA mode.

Table 1 presents the $\Delta G^{\gamma\to\varepsilon}$ values at room temperature (25°C) as calculated by Eq. (1). $\Delta G^{\gamma\to\varepsilon}$ decreased with decreasing Cr and Ni concentrations, which indicates an increase in the stability of ε-martensite against γ-austenite. Table 1 also presents the stacking fault energy (SFE) at room temperature, which is calculated as follows:

$$\Gamma_{\mathrm{SFE}} = 2\rho\Delta G^{\gamma\to\varepsilon} + 2\sigma^{\gamma/\varepsilon} \quad \text{..... (4)}$$

The SFE is calculated from the molar surface fraction on the γ plane ρ, $\Delta G^{\gamma\to\varepsilon}$, and the interfacial surface energy between the γ- and ε-phases $\sigma^{\gamma/\varepsilon}$. A detailed description of the SFE and the calculation of $\Delta G^{\gamma\to\varepsilon}$ are presented in the previous paper.[30] The effect of Si on the $\gamma\to\varepsilon$-martensitic transformation in the SFE or $\Delta G^{\gamma\to\varepsilon}$ calculation is given by the equation of Dumay *et al.*[36] Si has a nonlinear effect on the transformation and does not significantly affect the transformation temperature. However, it plays an important role in improving the plastic fatigue life.[37]

3.2. Experiments

DSC (TA Instrument Q-2000) was used to evaluate the martensitic transformation temperatures. Specimens were cut into dimensions of 3 mm × 3 mm × 0.4 mm with low-speed cutter. The measurement program was set as follows. Specimens were fully austenitized to 400°C and cooled to −150°C to measure the martensite start (M_s) and martensite finish (M_f) temperatures. Then they were heated to 400°C to measure the austenite start (A_s) and austenite finish (A_f) temperatures. The cooling and heating rates were both 20°C/min.

3.2.1. Low-cycle Fatigue Test

Axial strain-controlled fatigue tests were conducted at room temperature by using a hydraulic servo fatigue testing machine (MTS 370, MTS Systems Corporation, USA) equipped with a 250 kN load cell (661.22H-01, MTS Systems Corporation, USA). The gauge length of the extensometer (632.26F-20, MTS Systems Corporation) was 8 mm. A triangular test waveform was used with a strain rate of 0.4%/s and total strain amplitude of 1%. The specimens were machined so that the loading axis was parallel to the rolling axis. All tests were continued until specimen failure.

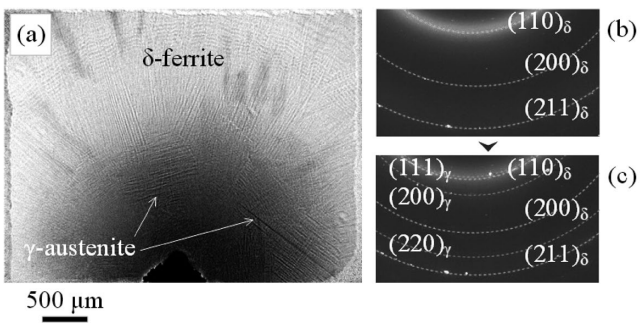

Fig. 1. Solidification sequence of Z5 during spot welding: (a) synchrotron radiation X-ray radiograph and diffraction patterns detected during (b) columnar dendrite growth and (c) equiaxial dendrite nucleation. (Online version in color.)

3.2.2. Microstructural Analysis

Microstructural analyses were conducted before and after fatigue tests via XRD (SmartLab, Rigaku Corporation, Japan), field-emission scanning electron microscopy (JEOL-7900F, JEOL Corporation, Japan) equipped with an EBSD detector (DVC5, TSL Corporation, Japan) and an EDS detector (JED-2300, JEOL Corporation, Japan), and a ferrite scope (FMP30, Fischer Technology Incorporated, USA). Specimens were cut from the as-heat-treated plate for analysis of the initial microstructure and from the parallel part of the fractured specimen for analysis of the deformed microstructures. The specimens were polished with waterproof papers up to #1200 followed by electropolishing by a solution of 70% perchloric acid (30 mL) with 99.5% ethanol (470 mL) for 600 s at 18 V and 15°C. The electropolishing removed approximately 45 μm of the thickness.

3.2.3. Corrosion Resistance

(1) Anodic Polarization Test

The anodic polarization test was performed by using a potentiostat (HABF-501A, Hokuto Denko Corp., Japan) connected to a function generator (HB-111, Hokuto Denko, Japan) with an analog cable. A silver–silver chloride (Ag/AgCl) electrode in a saturated KCl solution and a platinum electrode were used as the reference and counter electrodes, respectively. The specimens were cut by using a fine cutter into small pieces with dimensions of 10 mm × 10 mm, and the surfaces were wet-ground by using SiC water-resistant abrasive paper (KOVAX Corp., Japan). The surfaces were then finished by using #800 grit papers. The specimens were fixed in a polytetrafluoroethylene holder with an O-ring. The exposed area contacting the electrolyte was 0.35 cm^2 (6.7 mm in diameter). After the specimens were immersed in artificial seawater (SF-1, Osakayakken Co. Ltd., Japan) at 25°C under the open-air condition, the open circuit potential (OCP) was recorded for 30 min. Then, a gradient anodic potential was applied at a constant sweep rate of 20 mV min^{-1} from the initial potential of −100 mV from the final OCP value. The measurement was stopped when the current density limit of 1 mA cm^{-2} was recorded.

(2) Salt Spray Test

The salt spray test (SST) was performed according to the following procedure. Specimens were cut by a fine cutter into sheets approximately 1 mm in thickness, and the cross-sections were wet-ground with SiC water-resistant abrasive paper (KOVAX Corp., Japan). The surface was finished by using #800 grit paper. The sides and backside surfaces of the specimens were coated with insulating resin paint, which left a top surface area of 10 mm × 30 mm to ensure that only the target surface was in contact with the salt solution mist. The specimens were placed in the chamber of a salt spray testing machine (STP-30, Suga Test Instruments Co.,

Ltd., Japan) at a 70° horizontal angle. The test solution was 50 g L^{-1} NaCl aqueous solution, the test temperature was 35°C, and the amount of salt spray injected in the testing chamber was adjusted within the range of 18.75 ± 6.25 μL h^{-1} cm^{-2} (1.5 ± 0.5 mL h^{-1} for the 80 cm^2 aperture area of the horizontally placed collection vessel). After 24 h from the start of the test, the specimens were temporarily taken out, gently rinsed with pure water, and then dried quickly. Surface observation and morphology measurements were performed, followed by an additional 24 h of SST. The surface characterization was performed using a 3D optical/laser microscope (VR-3200, KEYENCE Corp., Japan).

4. Results

4.1. Differential Scanning Calorimetry

The martensitic transformation temperatures of M_s, A_s, and A_f were identified by using DSC. **Figure 2** shows the (a) colling- and (b) heating-DSC curves. **Table 2** lists the martensitic transformation temperatures. Our recent work confirmed that the transformation between γ-austenite and ε-martensite occurred during *in-situ* cooling XRD measurements in Fe-15Mn-10Cr-8Ni-4Si alloy.[30] Similarly, the same type of transformation, not involving α'-martensite, may occur in the present Fe–15Mn–aCr–bNi–4Si alloys at each transformation temperature measured by DSC. As shown in Fig. 2 and Table 2, the martensitic transformation temperatures increased with decreasing Cr and Ni concentrations or decreasing $\Delta G^{\gamma\to\varepsilon}$ and Γ_{SFE}. Z2 showed a small peak for only the heating curve, and Z1 did not show martensitic transformation peaks for both the cooling and heating curves. The M_s values of Z1 and Z2 were estimated by extrapolation of the trend for Z3–Z5 as −120 and −80°C, respectively. In the low temperature region, however, γ-austenite may be stabilized by the effect of Néel point,[34] resulting in lower M_s. If this is the case, sufficient driving force to continue the transformation cannot be obtained and the corresponding peak becomes weaker. Z4 and Z5 had relatively high M_s compared to Z1–Z3, and Z5 had a M_s over room temperature at 55.9°C. Therefore, reducing the Cr and Ni concentrations facilitated the martensitic transformation.

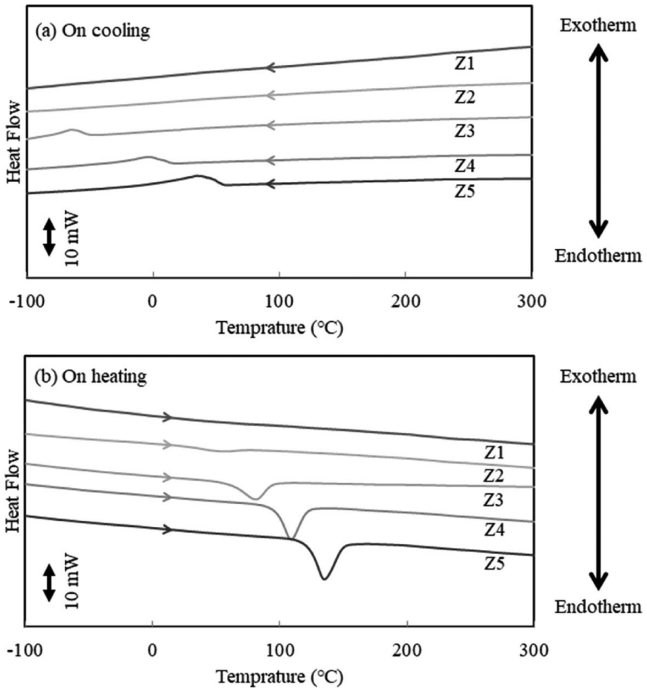

Fig. 2. DSC measurements during (a) cooling and (b) heating. (Online version in color.)

Table 2. Martensitic transformation temperature of the Fe–15Mn–aCr–bNi–4Si alloys [(a, b) = (14, 10.1), (12.5, 8.8), (11, 7.5), (9.5, 6.1), (8, 4.8)].

Alloy	M_s [°C]	A_s [°C]	A_f [°C]
Z1	ND	ND	ND
Z2	ND	ND	ND
Z3	−47.1	59.1	94.9
Z4	16.1	96.0	122.2
Z5	55.9	121.4	150.0

4.2. Initial Microstructure

The microstructure after heat treatment (*i.e.*, initial microstructure) was examined by XRD, EBSD, and a ferrite scope. **Figure 3** shows the XRD spectra for Z1–Z5. Some of the identified peaks were very weak and corresponded to ε-martensite in Z5 with high 2θ. Z1–3 had fully austenitic structures while Z4 and Z5 contained ε-martensite because of their high M_s. **Figure 4** shows the wide-field EBSD phase maps. As expected from the XRD results, Z1–Z3 had fully austenitic microstructures while Z4 and Z5 had a dual-phase microstructure comprising mostly γ-austenite with ε-martensite fractions of 3.5% and 25.6%, respectively. The grain sizes were measured counting high angle boundaries (> 15°) including the twin and γ/ε boundaries in the EBSD phase maps as 84.3 μm for Z1, 77.3 μm for Z2, 70.2 μm for Z3, 70.6 μm for Z4, and 57.2 μm for Z5. The specimens were examined by using the ferrite scope, but no α'-martensite was detected in any alloy.

4.3. Low-cycle Fatigue Test

Figure 5 shows that the fatigue lives N_f of the alloys strongly depended on their chemical compositions. Z2 had the highest N_f of 22 750 cycles at a total strain amplitude of 1%, which was twice that of Z3 (10 450 cycles) developed in the previous study. **Figure 6** shows the relationship

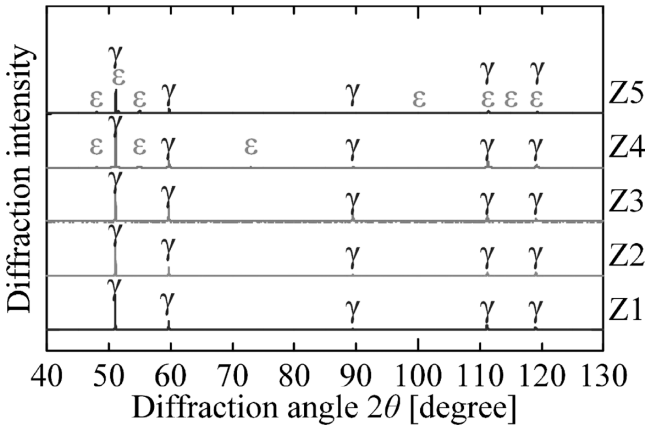

Fig. 3. X-ray diffraction spectra of Z1–Z5 after heat treatment. (Online version in color.)

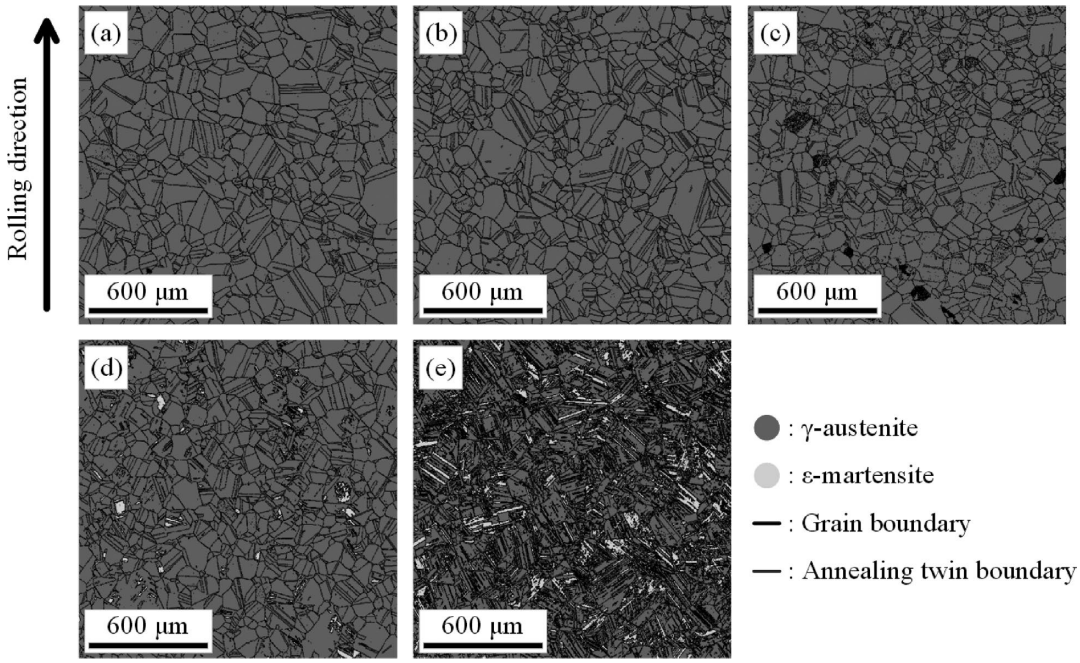

Fig. 4. Phase maps obtained by electron backscattering diffraction of (a) Z1, (b) Z2, (c) Z3, (d) Z4, and (e) Z5 after heat treatment. The field of view was 1.6 mm × 1.6 mm, and the step size was 2 μm. (Online version in color.)

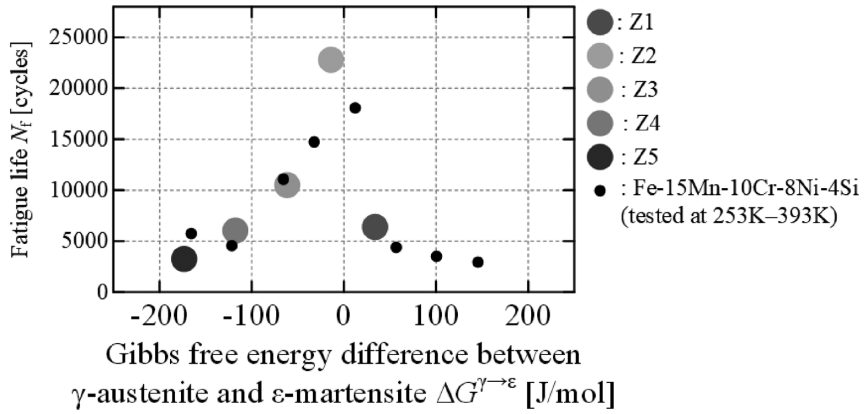

Fig. 6. Relationship between the fatigue life and Gibbs free energy difference between γ-austenite and ε-martensite $\Delta G^{\gamma\rightarrow\varepsilon}$ for Z1–Z5. The results obtained for Fe–15Mn–10Cr–8Ni–4Si at −20°C–120°C are also shown for comparison.[30] (Online version in color.)

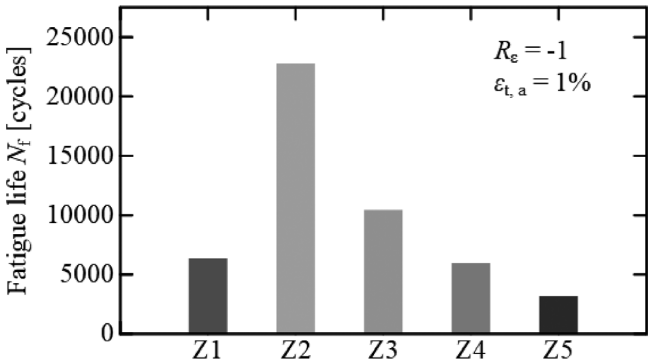

Fig. 5. Fatigue lives of Z1–Z5 at a strain ratio of −1 and total strain amplitude of 1%. (Online version in color.)

between N_f and $\Delta G^{\gamma\rightarrow\varepsilon}$ at room temperature. The results for Fe–15Mn–10Cr–8Ni–4Si, which was tested at different temperatures to obtain different $\Delta G^{\gamma\rightarrow\varepsilon}$, are also shown.[30] The same tendency was observed in the N_f–$\Delta G^{\gamma\rightarrow\varepsilon}$ relationship for both Fe–15Mn–10Cr–8Ni–4Si at different temperatures and for Z1–Z5 at room temperature: N_f took its maximum value near $\Delta G^{\gamma\rightarrow\varepsilon} = 0$, gradually decreased with decreasing $\Delta G^{\gamma\rightarrow\varepsilon}$ to approximately 5 000 cycles in the negative $\Delta G^{\gamma\rightarrow\varepsilon}$ regime, and rapidly decreased to below 5 000 cycles with increasing $\Delta G^{\gamma\rightarrow\varepsilon}$ in the positive $\Delta G^{\gamma\rightarrow\varepsilon}$ regime.

4.4. Microstructural Analysis

The deformation microstructure that developed after fatigue fracture (*i.e.*, post-fatigue microstructure) was investigated. The XRD measurements revealed that the post-fatigue microstructure comprised retained γ-austenite and deformation-induced martensite, as shown in **Fig. 7**. Some of the identified peaks were very weak. Z1 exhibited strong peaks for γ-austenite and weak peaks for ε-martensite. α'-martensite was detected in Z4 and Z5 but not in Z1–Z3.

Figure 8 shows the EBSD phase maps. In Z1, ε-martensite formed locally along the loading or rolling direction, as shown in Fig. 8(a). Figures 8(b)–8(e) show the corresponding EDS maps of Mn, Cr, Ni, and Si for Z1, where a brighter color corresponds to a higher concentration, and indicates

strong rolling segregation in Mn, Cr, and Ni. The distribution trends of Mn and Ni were in good agreement, while the Cr distribution was opposite. The rolling segregation varied a local $\Delta G^{\gamma\to\varepsilon}$ and may cause the local $\gamma\to\varepsilon$-martensitic transformation in the area with low $\Delta G^{\gamma\to\varepsilon}$ Figs. 8(c) and 8(d) show that the retained austenite in Z2 and Z3, respectively, was island-shaped and tended to be elongated along the rolling direction, which may also be attributed to the segregation. However, the effect of segregation is outside the scope of the present study. **Figure 9** shows the area fractions of each phase measured on the EBSD maps in Fig. 8. The fraction of ε-martensite increased with decreasing Cr and Ni concentrations, and Z4 and Z5 contained over 80% ε-martensite. Z2 and Z3 exhibited relatively large fractions of ε-martensite but also contained considerable amounts of retained austenite. Figure 9 show the fraction of α'-martensite measured by the ferrite scope. The fraction of α'-martensite increased with the Cr and Ni concentrations. No α'-martensite was detected in Z1. While XRD and EBSD did not identify any α'-martensite in Z2, the ferrite scope detected a small amount. Considerable amounts of α'-martensite were detected in Z4 and Z5.

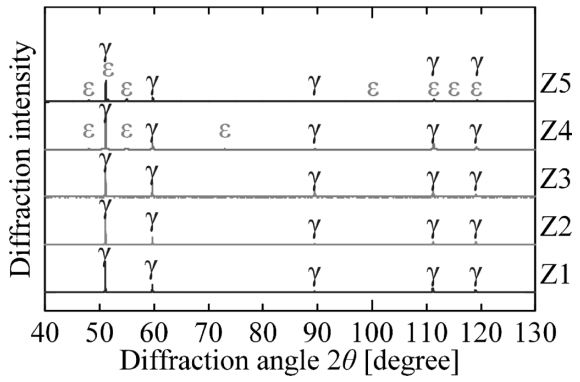

Fig. 7. X-ray diffraction spectra of Z1–Z5 after fatigue fracture. (Online version in color.)

4.5. Corrosion Resistance

Figure 10 shows the polarization curves of the specimens together with the reference carbon steel (JIS SM490A) in artificial seawater. The specimens had much nobler OCP values than the carbon steel. In addition, the current density of the specimens around the OCPs was apparently suppressed. These results indicate that the carbon steel was actively dissolved without forming any protective layer under the anodic polarization condition while the specimens were passivated. The base current density at the passive potential region was on the order of 10^{-6} A cm^{-2}, which is representative behavior of typical passivation-type corrosion-resistant alloys.[38] However, unstable current behavior indicating the transient occurrence of metastable

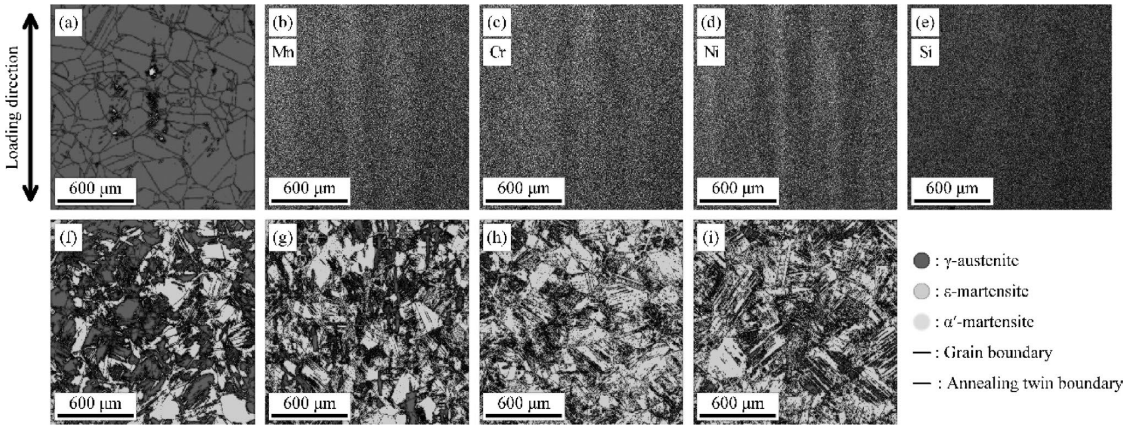

Fig. 8. Phase maps obtained by electron backscattering diffraction and Mn maps obtained by energy-dispersive X-ray spectroscopy after fatigue fracture: (a) EBSD and (b) Mn, (c) Cr, (d) Ni, and (e) Si EDS maps for Z1 and EBSD maps for (f) Z2, (g) Z3, (h) Z4, and (i) Z5. The EBSD had a field of view of 800 μm × 800 μm and a step size of 1 μm. (Online version in color.)

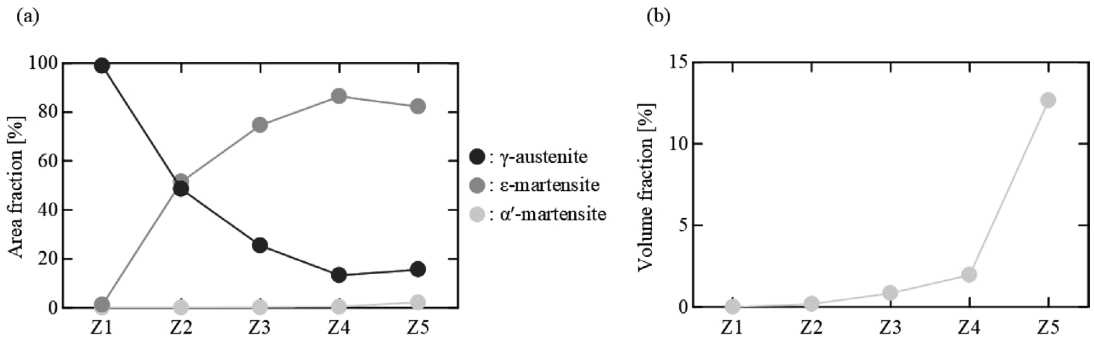

Fig. 9. Phase fractions in Z1–Z5 after fatigue fracture: (a) area fractions measured in the electron backscattering diffraction phase maps of Fig. 8 and (b) volume fractions of α'-martensite measured by the ferrite scope. The step size dependence of the phase fraction in the EBSD measurement in the present microstructure was confirmed to be small. (Online version in color.)

pitting corrosion and immediate re-passivation was frequently observed. At a potential of 0–0.2 V, breakdown of the passive film occurred, and stable corrosion pit propagation occurred. These results indicate that the specimens had superior corrosion resistance compared to carbon steel due to their passivation nature even in a seawater environment.

The changes in appearance of the specimens before and after SST are shown in **Fig. 11**(a). The pale-green insulating resin coating surrounding the area of the test surface demonstrated excellent adhesion and durability even after 48 h of testing. All specimen surfaces showed the formation of rust after 24 h of SST. For the carbon steel, a red-brown rust layer broadly developed and covered the surface. In contrast, the specimen surfaces showed local corroded sites, and the rust seemed to flow downward from the specimens placed in a standing position. Figure 11(b) shows the topographic profiles at the same observed locations. The rusted areas of the specimens had relatively concave pit shapes, and the rust precipitated around the pit. This indicates that these specimens were loosely passivated in the SST environment and that they exhibited localized corrosion. The appearance of these specimens remained almost unchanged after an additional 24 hours of SST. The corrosion pits may have been re-passivated by rinsing and drying for observation, so they were never reactivated in the additional testing period. In addition, these specimens showed almost no signs of new corrosion pits on their surfaces. In contrast, the carbon steel exhibited further corrosion during the additional testing period.

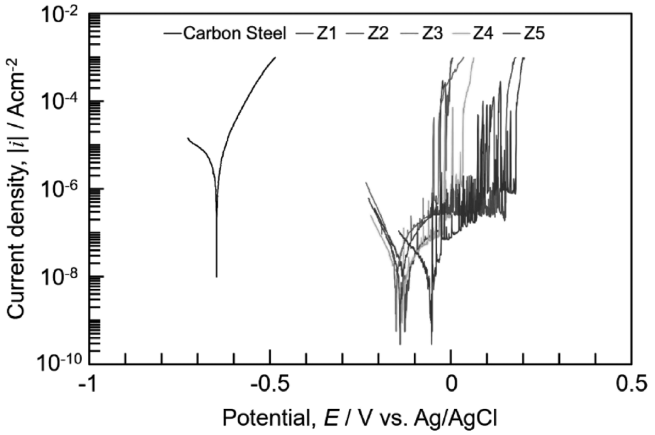

Fig. 10. Polarization curves of Z1–Z5. The curve for carbon steel (JIS SM490A) is also shown for comparison. (Online version in color.)

The change in surface roughness was measured for a quasi-quantitative evaluation of the degree of corrosion. The results are presented in **Table 3**. The surface roughness of the specimens before SST was generally at the same level, although there was only slight variation in the submicron order among the specimens. These differences were probably introduced not only by the intrinsic fine profile factor, but also by the macroscopic specimen shape like as the warpage and the waviness. The surface roughness tended to increase with the length of the testing period. It is due to the corrosion phenomena forming both the concave and convex areas: initiation/propagation of the corrosion pits and deposition of the corrosion products, respectively. The specimens showed a much smaller increase in roughness than the carbon steel. In addition, the increase in roughness was suppressed during the additional 24-h testing period compared to the initial 24-h period. The degree of the roughness increase was smaller among specimens with higher Cr and Ni concentrations. Therefore, these elements were concluded to help enhance the corrosion resistance of

Table 3. Changes in arithmetic surface roughness, Sa (μm) of the specimens before and after the salt spray test.

Alloy	Z1	Z2	Z3	Z4	Z5	Carbon steel
Before SST	0.6	0.5	0.9	0.4	0.5	0.4
After SST (24 h)	0.9	0.8	1.3	1.9	2.9	27.7
After SST (48 h)	1.1	1.0	1.5	2.3	3.6	52.7

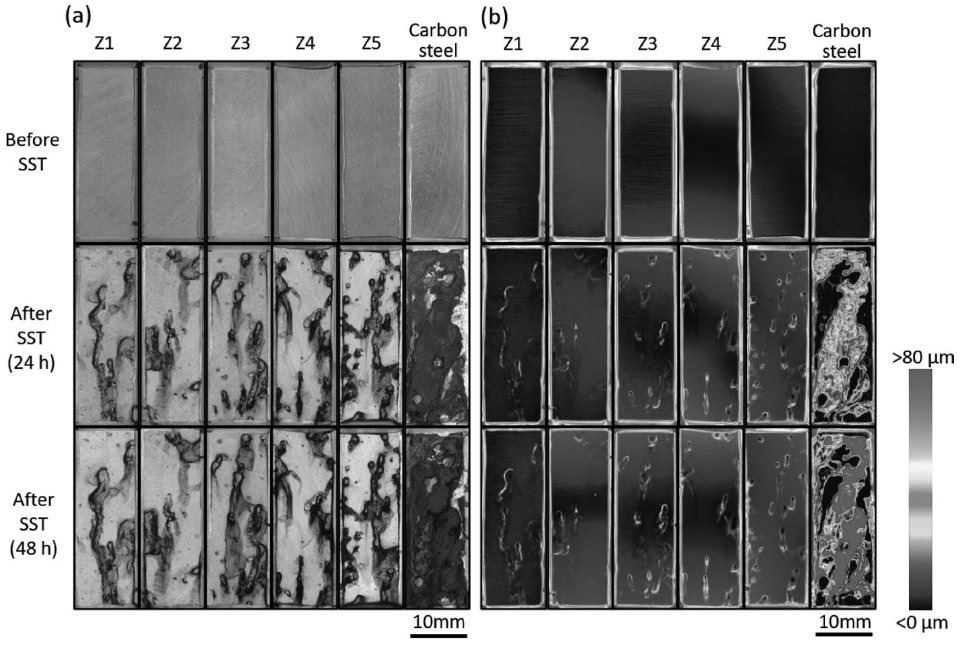

Fig. 11. Appearance of specimens before and after salt spray test. (Online version in color.)

the developed alloys.

5. Discussion

The fatigue life N_f of the Fe–Mn–Cr–Ni–Si alloys strongly depended on the Cr and Ni concentrations. N_f was 3 197 cycles for Z5 and 22 750 cycles for Z2. The difference in N_f can be explained by the deformation mechanism based on $\Delta G^{\gamma\to\varepsilon}$. As shown in Fig. 6, the relationship between N_f and $\Delta G^{\gamma\to\varepsilon}$ showed the same trend for Z1–Z5 as for the previously developed alloy Fe–15Mn–10Cr–8Ni–4Si at various temperatures:[30] N_f is maximum at $\Delta G^{\gamma\to\varepsilon} \approx 0$, gradually decreases with decreasing $\Delta G^{\gamma\to\varepsilon}$ in the negative $\Delta G^{\gamma\to\varepsilon}$ regime, and rapidly decreases with increasing $\Delta G^{\gamma\to\varepsilon}$ in the positive $\Delta G^{\gamma\to\varepsilon}$ regime. These results indicate that both the effects of chemical composition and test temperature on the Fe–Mn–Cr–Ni–Si alloy system can be evaluated by using $\Delta G^{\gamma\to\varepsilon}$ to characterize the deformation mechanism. The effects of the Cr and Ni concentrations on the fatigue life can thus be discussed together using $\Delta G^{\gamma\to\varepsilon}$ rather than individually. Z2 exhibited the longest N_f of over 20 000 cycles, which was twice that of the previously developed Z3 (over 10 000 cycles), which itself also had an extraordinary long N_f compared to conventional steels (about 2 000 cycles).[6] Z2 and Z3 had $\Delta G^{\gamma\to\varepsilon}$ of −13.4 and −61.0 J/mol, respectively. A negative near-zero $\Delta G^{\gamma\to\varepsilon}$ value is favorable for the B-TRIP mechanism.[18,30] The high N_f of both Z2 and Z3 indicates the effectiveness of the B-TRIP mechanism at increasing fatigue resistance. Z2 has a $\Delta G^{\gamma\to\varepsilon}$ value closer to zero than Z3, so it has a smaller potential that must be overcome to reversely transform from ε-martensite to γ-austenite. The smaller fraction of ε-martensite in Z2 compared to Z3 shown in Fig. 9(a) implies the frequent occurrence of the reverse transformation. The easier occurrence of the B-TRIP mechanism in Z2 may significantly mitigate damage accumulation during cyclic loadings. However, it is possible that the low amount of ε-martensite in Z2 compared to that in Z3 is a result of the stabilization of γ-austenite and suppression of the $\gamma\to\varepsilon$ martensitic transformation due to the increase in Mn content, as well as the reverse transformation. It is also worth noting that the moderate suppression of the $\gamma\to\varepsilon$ transformation in Z2, as compared to Z3, may have contributed to the improvement in fatigue durability in Z2. Further research is needed to fully understand the effect of the $\gamma\to\varepsilon$ transformation or the formation and deformation of ε-martensite on fatigue life. Additionally, the fraction of α'-martensite was larger in Z3 than in Z2. In the $\gamma\to\varepsilon$ martensitic transformation, the reverse $\varepsilon\to\gamma$ transformation occurs due to the inverse motion of the Schockley partial dislocation, but this reverse transformation mechanism does not operate in the $\gamma\to\alpha'$ martensitic transformation because of a large amount of slip introduced by the lattice-invariant deformation. Additionally, sufficient driving force for the reverse transformation cannot be obtained since the thermal equilibrium temperature in the $\gamma\to\alpha'$ martensitic transformation is higher than that in the $\gamma\to\varepsilon$ martensitic transformation. Therefore, the large fraction of α'-martensite in Z3 can explain the reduced N_f compared to Z2, where the α'-martensitic transformation was suppressed well.

Z1 exhibited a smaller N_f than Z2 due to the deviation of its $\Delta G^{\gamma\to\varepsilon}$ value, which is not conducive to the B-TRIP mechanism. However, it still had a greater N_f than that reported for conventional steels. Mughrabi pointed out that the occurrence of cross-slip reduces the reversibility of dislocation motions because the reverse glide of dislocations cannot occur on the same slip plane with the forward glide once cross-slip has occurred.[19] Z1 had a low Γ_{SFE} of 21.04 mJ/m^2, which indicates that dislocations can easily extend and cross-slip is suppressed. The high reversibility of the extended dislocation motion may be responsible for the relatively long N_f of Z1 even though it does not follow the B-TRIP mechanism.

The dominant deformation mechanism in Z4 and Z5 might be stress-assisted ε-martensitic transformation, which can be attributed to their high M_s. The large fractions of ε-martensite as shown in Figs. 8 and 9 also indicate the high tendency for ε-martensitic transformation. The gradual decrease in N_f with decreasing $\Delta G^{\gamma\to\varepsilon}$ in the negative $\Delta G^{\gamma\to\varepsilon}$ regime (Z2–Z5) may be attributed to the reduction in the frequency of bidirectional transformation. Z4 and Z5 had a lower Γ_{SFE} than Z2 and Z3, which implies that their dislocation motion was more reversible. Meanwhile, ε-martensite is considered a brittle phase that causes premature fracture.[39,40] The poor tendency for reversible $\varepsilon\to\gamma$ transformation and the detrimental effect of ε-martensite may be responsible for the reduced N_f of Z4 and Z5 compared to Z2 and Z3.

As shown in Figs. 10 and 11, the developed alloys exhibited much better corrosion resistance than carbon steel due to passivation. The developed alloys demonstrated localized corrosion behavior in an artificial seawater: breakdown of the passivated film and localized pitting corrosion. Stainless steel is defined as containing more than 10.5% Cr.[41] It is interesting that the compositions of Z4 and Z5 in this study did not satisfy this requirement, although they showed localized corrosion behavior due to the spontaneous formation of passive film. The pitting corrosion may occur at MnS-type inclusions caused by the high Mn concentration of 15 wt%. In the case of stainless steels processings, the Mn and S concentrations are limited to improve the pitting corrosion resistance.[42] In fact, detrimental effect of high content of Mn on corrosion resistance of stainless steel was reported.[43] On the other hand, the addition of Si to stainless steels has also been found to improve corrosion resistance.[44,45] Therefore, the superior corrosion resistance of the specimens with relatively lower Cr and high Mn content, such as Z4 and Z5, is considered to be due to the enhancement effect on passive film formation by Si. In our earlier study, Nishimura[46] reported that the passivation films formed on the steel with similar compositions to those in this study consisted of two-layer structure with an Si-enriched inner layer. While pitting corrosion occurred during the SST, the increase in the number of pits seemed to saturate after 24 h. Additionally, most of the corrosion pits were re-passivated, which prevented the corrosion from proceeding further. The number of pits tended to decrease with increasing Cr and Ni concentrations. Z1 and Z2 had the first and second highest Cr and Ni concentrations and exhibited fewer corrosion pits as well as a smaller change in surface roughness than the previously developed Z3. Therefore, the developed alloys demonstrated pitting corrosion that can be attributed to the high Mn concentration, but presence of Si and increasing

the Cr and Ni concentrations helped improve the corrosion resistance.

6. Conclusion

The fatigue and corrosion resistant alloy were newly developed by optimizing Cr and Ni concentrations, by adapting the design concept for fatigue resistant alloy based on bidirectional TRIP (B-TRIP). Compared with the previously developed damping steel Fe–15Mn–10Cr–8Ni–4Si and Fe-15Mn-11Cr-7.5Ni-4Si (Z3), newly developed 15Mn–12.5Cr–8.7Ni–4Si alloy (Z2), slightly increasing the Cr and Ni concentrations optimized $\Delta G^{\gamma\rightarrow\varepsilon}$ to increase N_f twofold. Increasing the Cr and Ni concentrations simultaneously increased the corrosion resistance. During SST, the developed alloys exhibited pitting corrosion that can be attributed to the high Mn concentration, so their application in harsh corrosive environments should be carefully considered. However, the improved corrosion resistance of Z2 compared to Z3 indicates that increasing the Cr and Ni concentrations can extend the range of applications of fatigue-resistant steel alloys. Future work will involve improving the corrosion resistance of these alloys, such as by reducing the Mn concentration, while maintaining the excellent fatigue resistance and weldability.

Acknowledgments

We would like to acknowledge the assistance provided by the Materials Manufacturing and Engineering Station, NIMS, for material processing. We also acknowledge the support of a NEDO Leading Research Program (JPNP14004) from the New Energy and Industrial Technology Development Organization (NEDO), Japan. A part of this work was supported by a Grant-in-Aid for Early-Career Scientists (21H01659, 23K13227) from the Japan Society for the Promotion of Science (JSPS), Japan.

REFERENCES

1) B. Spencer, Jr. and S. Nagarajaiah: *J. Struct. Eng.*, **129** (2003), 845. https://doi.org/10.1061/(ASCE)0733-9445(2003)129:7(845)
2) D. R. Teruna, T. A. Majid and B. Budiono: *Adv. Civil. Eng.*, **2015** (2015), 1. https://doi.org/10.1155/2015/631726
3) C. Fang, W. Wang, Y. Ji and M. C. Yam: *J. Const. Steel. Research.*, **184** (2021), 106817.
4) I. Nikulin, T. Sawaguchi, A. Kushibe, Y. Inoue, H. Otsuka and K. Tsuzaki: *Int. J. Fatigue.*, **88** (2016), 132. https://doi.org/10.1016/j.ijfatigue.2016.03.021
5) F. Yoshinaka, T. Sawaguchi, S. Takamori, S. Emura and Y. Inoue: *Int. J. Fatigue*, **171** (2023), 107581. https://doi.org/10.1016/j.ijfatigue.2023.107581
6) F. Yoshinaka, T. Sawaguchi, S. Takamori, T. Nakamura, G. Arakane, Y. Inoue, S. Motomura and A. Kushibe: *Scripta Mater.*, **197** (2021), 113815. https://doi.org/10.1016/j.scriptamat.2021.113815
7) K. Hatanaka: *JSME International Journal. Ser. 1, Solid Mechanics, Strength of Materials*, **33** (1990), 13. https://doi.org/10.1299/jsmea1988.33.1_13
8) T. Hilditch, H. Beladi, P. Hodgson and N. Stanford: *Mater. Sci. Eng. A.*, **534** (2012), 288. https://doi.org/10.1016/j.msea.2011.11.071
9) Y. Wen, H. Peng, D. Raabe, I. Gutiérrez-Urrutia, J. Chen and Y. Du: *Nature Com.*, **5** (2014), 4964. https://doi.org/10.1038/ncomms5964
10) C. Shao, P. Zhang, R. Liu, Z. Zhang, J. Pang and Z. Zhang: *Acta Mater.*, **103** (2016), 781. https://doi.org/10.1016/j.actamat.2015.11.015
11) C. Shao, P. Zhang, R. Liu, Z. Zhang, J. Pang, Q. Duan and Z. Zhang: *Acta Mater.*, **118** (2016), 196. https://doi.org/10.1016/j.actamat.2016.07.034
12) W. Tasaki, T. Sawaguchi, I. Nikulin, K. Sekido and K. Tsuchiya: *Mater. Trans.*, **57** (2016), 639. https://doi.org/10.2320/matertrans.MBW201503
13) M. W. Klein, M. Smaga and T. Beck: *Metals*, **8** (2018), 832. https://doi.org/10.3390/met8100832
14) K. Lu, A. Chauhan, M. Walter, A. S. Tirunilai, M. Schneider, G. Laplanche, J. Freudenberger, A. Kauffmann, M. Heilmaier and J. Aktaa: *Scripta Mate.*, **194** (2021), 113667. https://doi.org/10.1016/j.scriptamat.2020.113667
15) S. A. A. Shams, J. W. Bae, J. N. Kim, H. S. Kim, T. Lee and C. S. Lee: *J. Mater. Sci. Technol.*, **115** (2022), 115. https://doi.org/10.1016/j.jmst.2021.10.010
16) W. Lu, C. H. Liebscher, G. Dehm, D. Raabe and Z. Li: *Adv. Material.*, **30** (2018), 1804727. https://doi.org/10.1002/adma.201804727
17) F. Yoshinaka, T. Sawaguchi, S. Takamori and S. Emura: *Materi. Sci. Eng. A*, **833** (2022), 142583. https://doi.org/10.1016/j.msea.2021.142583
18) T. Sawaguchi, Y. Tomota, F. Yoshinaka and S. Harjo: *Acta Mater.*, **242** (2023), 118494. https://doi.org/10.1016/j.actamat.2022.118494
19) H. Mughrabi: *Metall. Mater. Trans. B*, **40** (2009), 431. https://doi.org/10.1007/s11663-009-9240-4
20) F. Bahadur, R. Jain, K. Biswas and N. Gurao: *Int. J. Fatigue*, **155** (2022), 106545. https://doi.org/10.1016/j.ijfatigue.2021.106545
21) T. Sawaguchi, T. Maruyama, H. Otsuka, A. Kushibe, Y. Inoue and K. Tsuzaki: *Mater. Trans.*, **57** (2016), 283. https://doi.org/10.2320/matertrans.MB201510
22) Y. Inoue, A. Kushibe, K. Umemura, Y. Mizushima, T. Sawaguchi, T. Nakamura, H. Otsuka and Y. Chiba: *J. Arc. Review*, **4** (2021), 76. https://doi.org/10.1002/2475-8876.12193
23) D. A. Jones: Principles and Prevention, Corrosion, 2 (1996), 168.
24) R. Ebara: *Procedia Eng.*, **2** (2010), 1297. https://doi.org/10.1016/j.proeng.2010.03.141
25) M. Amirifard, A. Z. Hanzaki, H. Abedi, N. Eftekhari and Q. Wang: *J. Mater. Res. Technol.*, **17** (2022), 1672. https://doi.org/10.1016/j.jmrt.2022.01.109
26) V. Urban, V. Krivy and K. Kreislova: *Proc. Eng.*, **114** (2015), 546. https://doi.org/10.1016/j.proeng.2015.08.104
27) K. J. Kere and Q. Huang: *J. Bridge Eng.*, **24** (2019), 04019007. https://doi.org/10.1061/(ASCE)BE.1943-5592.0001361
28) M. H. Hebdon and J. T. Provines: *J. Perform. Const. Facil.*, **34** (2020), 04020108. https://doi.org/10.1061/(ASCE)CF.1943-5509.0001498
29) H. Iken, R. Basseguy, A. Guenbour and A. B. Bachir: *Electro. Acta*, **52** (2007), 2580. https://doi.org/10.1016/j.electacta.2006.09.013
30) T. Sawaguchi, I. Nikulin, K. Ogawa, S. Takamori, F. Yoshinaka, Y. Chiba, H. Otsuka, Y. Inoue and A. Kushibe: *Acta Mater.*, **220** (2021), 117267. https://doi.org/10.1016/j.actamat.2021.117267
31) S. Katayama, T. Fujimoto and A. Matsunawa: Correlation among Solidification Process, Microstructure, Microsegregation and Solidification Cracking Susceptibility in Stainless Steel Weld Metals (Materials, Metallurgy & Weldability), 14 (1985). https://doi.org/10.18910/10942
32) J. Lippold: Solidification Behavior and Cracking Susceptibility of Pulsed-laser Welds in Austenitic Stainless Steels, Welding Journal Including Welding Research Supplement, 73 (1994), 129s.
33) P. Guiraldenq and O. Hardouin Duparc: *Metall. Res. Technol.*, **114** (2017), 613. https://doi.org/10.1051/metal/2017059
34) T. Nagira, T. Nakamura, F. Yoshinaka, T. Sawaguchi, Y. Aoki, M. Kamai, H. Fujii, A. Takeuchi and M. Uesugi: *Scripta Mater.*, **216** (2022), 114743. https://doi.org/10.1016/j.scriptamat.2022.114743
35) T. Nagira, T. Nakamura, T. Kimura, F. Yoshinaka, T. Sawaguchi, T. Yamashita, Y. Aoki and H. Fujii: *Quarterly Journal of the Japan Welding Society*, **41** (2023), 1s. https://doi.org/10.2207/qjjws.41.1s
36) A. Dumay, J.-P. Chateau, S. Allain, S. Migot and O. Bouaziz: *Sci. Eng. A*, **483** (2008), 184. https://doi.org/10.1016/j.msea.2006.12.170
37) I. Nikulin, T. Sawaguchi, K. Ogawa and K. Tsuzaki: *Acta Mater.*, **105** (2016), 207. https://doi.org/10.1016/j.actamat.2015.12.002
38) Y. Tsutsumi, S. Bartáková, P. Prachár, S. Migita, H. Doi, N. Nomura and T. Hanawa: *J. Electro. Soc.*, **159** (2012), C435. https://doi.org/10.1149/2.045210jes
39) M. Koyama, T. Sawaguchi and K. Tsuzaki: *Metall. Mater. Trans. A*, **43** (2012), 4063. https://doi.org/10.1007/s11661-012-1220-7
40) F. Yoshinaka and T. Sawaguchi: *Int. J. Fatigue*, **130** (2020), 105271. https://doi.org/10.1016/j.ijfatigue.2019.105271
41) ISO 15510: 2014, Stainless steels -- Chemical composition.
42) A. Chiba, I. Muto, Y. Sugawara and N. Hara: *J. Electro. Soc.*, **160** (2013), C511. https://doi.org/10.1149/2.081310jes
43) R. F. A. Jargelius-Pettersson: *ISIJ Int.*, **36** (1996), 818. https://doi.org/10.2355/isijinternational.36.818
44) W. T. Tsai, Y. N. Wen, J. T. Lee, H. Y. Liou and W. F. Wang: *Surf. Coat. Tech.*, **34** (1988), 209. https://doi.org/10.1016/0257-8972(88)90113-2
45) R. Nishimura, K. Yamakawa, J. Ishiga, Y. Matsumoto and H. Nagano: *Mater. Chem. Phys.*, **54** (1998), 289. https://doi.org/10.1016/S0254-0584(98)00104-7
46) T. Nishimura: *Mater. Trans.*, **55** (2014), 871. https://doi.org/10.2320/matertrans.M2014029